PNAS RESEARCH ARTICLE | APPLIED BIOLOGICAL SCIENCES ENGINEERING

Amplification-free dual-blocking autocatalytic CRISPR-Cascade for attomolar DNA detection with low nonspecific signal

Jongwon Lim[a,b,c], An Bao Van[a,b], Matthew Wester[a,b], Katherine Koprowski[a,b], Enrique Valera[a,b,d], and Rashid Bashir[a,b,d,e,f,g,h,i,1]

Affiliations are included on p. 11.

Edited by Jeffrey Alan Hubbell, New York University, New York, NY; received December 23, 2025; accepted April 27, 2026

Autocatalytic CRISPR architecture offers amplification-free nucleic acid detection by directly linking target recognition to self-reinforcing ribonucleoprotein (RNP) generation. However, spontaneous background activation remains a key barrier, because strand invasion or unwinding events can initiate unintended amplification and diminish assay specificity. Here, we introduce a dual-blocking CRISPR-Cascade design that independently cages both the guide RNA and trigger DNA, establishing an intrinsic AND gate to raise the effective kinetic barrier for unintended RNP formation. This strategy suppresses leakage by approximately 3- to 18-fold relative to single blocking configurations in full Cascade reactions, while preserving rapid detection (10 min), achieving single-copy sensitivity, and enabling quantitative detection. When paired with a competitive guide RNA decoy, the system further reduces background signals without affecting true target detection. Finally, we demonstrate robust Methicillin-resistant *Staphylococcus aureus* detection from whole blood in under 40 min including the sample purification and extraction. These results establish dual-blocking as a generalizable molecular gating framework for constructing leakage-resistant, amplification-free CRISPR systems suitable for rapid and decentralized diagnostics.

autocatalytic CRISPR | amplification-free CRISPR detection | molecular gating | nucleic acid diagnostics | positive feedback circuits

Significance

Amplification-free CRISPR diagnostics are often described as simple positive feedback circuits, yet background noise signal from target-independent activation can be undesirably high. Existing approaches treat these background "leakage" signals as unavoidable, without addressing key sources such as Cas-driven strand invasion and transient duplex respiration. Here, we analyze these pathways using switchable caged gRNA (scgRNA) and Cascade probes, showing that single-component blocking is inherently vulnerable. We introduce a dual-blocking strategy that gates both guide RNA and trigger DNA, combined with a decoy gRNA strategy. This multilayer design suppresses background activation and improves signal-to-noise, establishing a general principle for constructing robust amplification-free CRISPR circuits.

Nucleic acid diagnostics traditionally rely on PCR or other target amplification methods to achieve high sensitivity (1, 2). Although highly effective, these workflows require multistep sample processing, precise temperature control, and pose a risk of carryover contamination, making them less suitable for rapid or decentralized testing (3). CRISPR-based detection systems have addressed several of these limitations by offering programmable target recognition and operation under isothermal reaction conditions (4, 5). However, most CRISPR-based assays are limited to approximately picomolar (pM) detection without an upstream nucleic acid amplification step, while attomolar (aM) sensitivity is required for clinical relevance (6–8).

To eliminate this dependency, autocatalytic CRISPR architectures have recently emerged as a strategy to couple target recognition directly to self-reinforcing ribonucleoprotein (RNP) activation (9). In these systems, the key molecules are called blocked nucleic acids (BNAs) or autocatalytic nucleic acids (ANAs), which are switchable intermediates or blocked precursors. An initial target-activated Cas complex converts inactive BNAs into new active enzymes, forming a positive feedback loop that enables exponential signal gain without thermal cycling (10–12). Several BNA designs have been developed to achieve conditional activation, including cleavage-activated guide-releasing constructs (9), intramolecularly folded trigger strands stabilized by nucleic-acid chemistries (13, 14), duplex-protected DNA/RNA triggers (15), and topology-gated circular nucleic acids that are linearized by cleavage (16). However, each of these systems blocks only one of the Cas-activating components (gRNA or target nucleic acid) and typically provides the other in excess. Collectively, these approaches demonstrate that nucleic-acid structures can be programmed to serve as feedback gates that drive self-catalyzing CRISPR reaction.

Despite these advances, all existing autocatalytic CRISPR systems share a fundamental challenge: spontaneous background activation (11, 12). Transient equilibrium fluctuations of BNA, or strand-invasion-driven unwinding by Cas enzymes can generate small amounts of active RNPs that propagate through the positive feedback loop. This leakage causes fluorescence accumulation in the absence of target, narrows the dynamic range, limits quantification, complicates thresholding, and ultimately limits confidence at low target concentrations, precisely where amplification-free systems offer the greatest potential impact.

Author contributions: J.L., M.W., E.V., and R.B. designed research; J.L., A.B.V., M.W., and K.K. performed research; J.L. contributed new reagents/analytic tools; J.L., A.B.V., and M.W. analyzed data; and J.L., A.B.V., M.W., K.K., E.V., and R.B. wrote the paper.

Competing interest statement: R.B. has financial interests in VedaBio, Inc.

This article is a PNAS Direct Submission.

Copyright © 2026 the Author(s). Published by PNAS. This article is distributed under Creative Commons Attribution-NonCommercial-NoDerivatives License 4.0 (CC BY-NC-ND).

[1]To whom correspondence may be addressed. Email: rbashir@illinois.edu.

This article contains supporting information online at https://www.pnas.org/lookup/suppl/doi:10.1073/pnas.2537414123/-/DCSupplemental.

Published May 21, 2026.

To overcome this limitation, we developed a dual-blocking architecture that simultaneously cages the guide RNA (gRNA) and the trigger DNA required to form the amplifying Cas12a complex (Fig. 1). Productive RNP assembly, and thus initiation of the feedback loop, requires coordinated release of both components, enforcing an intrinsic AND-gate logic at the core of autocatalytic activation. This design establishes two orthogonal kinetic barriers against unintended RNP formation (Fig. 1*A*), substantially elevating the activation threshold relative to single-blocking systems. To further suppress rare leakage events, we also introduce a sacrificial guide RNA decoy that competitively occupies free Cas enzymes before they can engage the blocked substrates. Together, these strategies lower the negative baseline signal while preserving rapid exponential amplification upon target recognition, enabling sensitive, target-amplification-free detection with greatly reduced false activation risk. Using this architecture, we demonstrate rapid and specific detection of MRSA, including successful identification of low-copy targets obtained through extraction and purification from whole blood samples.

Results

Rationale for Dual-Blocking of Autocatalytic CRISPR-Cascade Reaction Systems. Autocatalytic CRISPR reactions enable highly sensitive detection but are often compromised by spontaneous background amplification caused by unintended activation of the positive feedback loop. The CRISPR-Cascade reaction is initiated when RNP T1, formed when Cas12a is precomplexed with a target-specific gRNA, recognizes and cis-cleaves target DNA, activating indiscriminate trans-cleavage (Fig. 1*B*). Activated RNP T1 then triggers the downstream autocatalytic reaction by converting latent precursors into active components of RNP T2.

Previous BNA designs have relied on a single-blocking strategy in which only one precursor species was protected to create a switchable intermediate. Specifically, a switchable caged guide RNA (scgRNA, Fig. 1*C*) and Cascade probe (CP, Fig. 1*D*) are preassembled by blocking the gRNA and trigger DNA, respectively, and are supplied in the RNP T2 tube as switchable precursors. In both approaches, engineered single-stranded DNA (ssDNA) bulges act

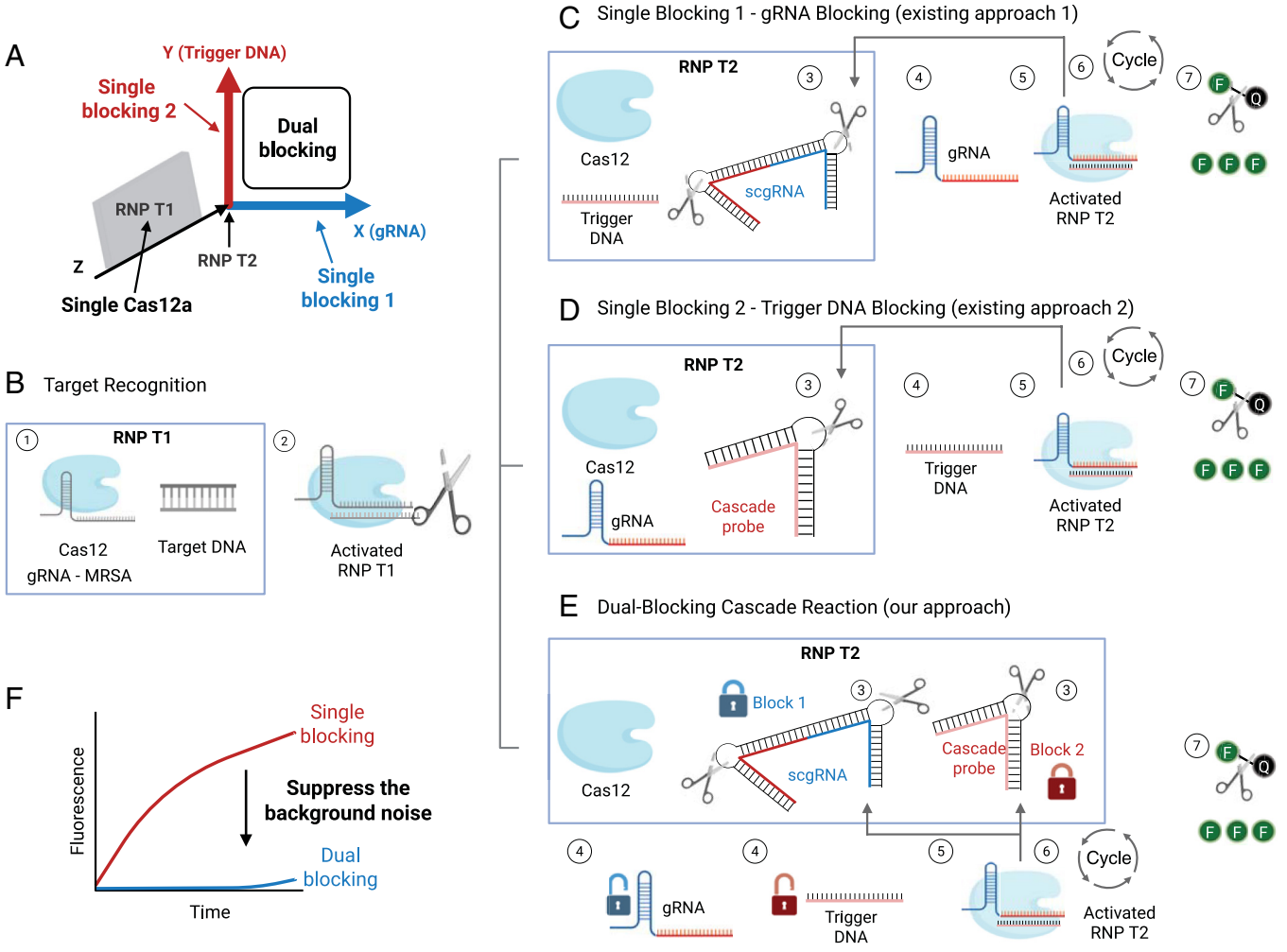


Fig. 1. Dual-blocking strategy for suppressing background signals in autocatalytic CRISPR-Cascade reactions. (*A*) The AND-gate logic imposes two orthogonal thermodynamic and kinetic barriers to spontaneous activation, reducing leakage and nonspecific background relative to single-blocking systems. Activated RNP T1 feeds into the RNP T2 autocatalytic module. Blocking can be applied either on the gRNA axis (single blocking 1) or on the trigger-DNA axis (single blocking 2), and both can be applied simultaneously at their intersection to implement dual-blocking. The Cascade mechanism is modularized into (*B*) primary target recognition (RNP T1) and (*C*–*E*) downstream signal amplification (RNP T2). (*B*) RNP T1 becomes activated upon binding and cleaving target DNA. (*C* and *D*) In single-blocking configurations, either the switchable caged guide RNA (scgRNA for gRNA-blocking) or Cascade probe (trigger-blocking) protects one precursor. Activated RNP T1 cleaves the bulge structures to release either gRNA or trigger DNA, enabling RNP T2 formation and self-amplifying positive feedback. (*E*) In our dual-blocking approach, both precursors are caged, requiring two independent unlock steps before RNP T2 assembly, thus elevating the activation threshold and limiting leakage. (*F*) The dual-blocking approach can markedly reduce spontaneous background fluorescence compared to single blocking.

as conditional gates; cleavage of the bulge by activated RNP T1 releases the guide RNA or trigger DNA, which in turn increases the number of activated RNP T2 and reinforces the autocatalytic loop. Here, it is important to note that the corresponding unprotected strand (e.g., trigger DNA for scgRNA systems and gRNA for Cascade-probe systems) is provided in high concentration (tens to hundreds of nanomolar) in the RNP T2 mixture. Consequently, once the trans-cleavage activity of activated RNP T1 cleaves the BNA bulges and releases small amounts of active gRNA or trigger DNA, RNP T2 complexes form rapidly, thereby initiating and amplifying the autocatalytic feedback loop.

However, single-blocking systems often fail to suppress nonspecific background signals due to two intrinsic leakage mechanisms arising from: i) Cas enzyme–driven strand invasion and ii) transient base-pair "respiration" of blocked BNA duplexes at thermodynamic equilibrium. In the first case, Cas12a can spontaneously invade and open scgRNA to form functional RNP complexes, or preassembled RNPs can intermittently strand-invade and unwind Cascade probes, transiently activating the feedback loop through unintended RNP T2 formation (*SI Appendix*, Fig. S1 *A* and *B*) (17, 18). In the second case, the coexistence of unlocked and blocked BNA species at thermodynamic equilibrium allows partial exposure of the recognition site, promoting stochastic initiation events (*SI Appendix*, Fig. S1 *C* and *D*) (19, 20). Together, these two mechanisms synergistically contribute to background nonspecific signals in single-blocking systems. A detailed theoretical justification for this behavior, including derivation of how thermodynamic leakage is predicted to scale with the annealed fraction at equilibrium and why dual-blocking yields multiplicative suppression of the assay background, can be found in *SI Appendix, Supplementary Note 1 Dual-Blocking Rationale*.

To minimize these leakage effects, we developed a dual-blocking system that involves blocking both the gRNA and trigger DNA using the scgRNA and Cascade probe (Fig. 1*E*). Upon target recognition, RNP T1 cleaves the ssDNA bulges in both constructs, releasing unblocked gRNA and trigger DNA, and enabling productive formation of RNP T2 (13). This architecture therefore requires both BNA components to be activated, implementing an AND-logic gate, and imposing two orthogonal kinetic barriers to spontaneous activation by independently caging both gRNA and trigger DNA (Fig. 1*A*). As a result, the dual-blocking architecture markedly suppresses background noise compared to the single-blocking approach (Fig. 1*F*).

Construction and Baseline Evaluation of Dual-Blocking Components. To construct the dual-blocking system, we first adapted a scgRNA architecture in which the gRNA is hybridized with two inhibitor DNAs, iDNA-handle (iH) and iDNA-spacer (iS), following the design of Shi et al. (Fig. 2*A*) (9). The spacer region of gRNA was used to define the trigger DNA (TD) sequence, and its complementary strand was engineered into a bubble DNA (BD) containing a seven-base single-stranded bulge (TTTATTT) at the middle location of the bubble DNA to generate a Cascade probe that cages the trigger DNA (Fig. 2*B*). Thermodynamic predictions from NUPACK (21) and DINAMelt (22) indicated stable secondary structures for both scgRNA and the Cascade probe (*SI Appendix*, Fig. S2 *A*–*C*). Experimental validation using melting curve analysis and native 15% PAGE confirmed correct formation of both blocked complexes (scgRNA and CP) from individual components (iH, iS, gRNA, TD, BD), consistent with simulation output (Fig. 2 *C* and *D*).

To quantify the blocking effect of BNA independent from upstream activation, we implemented a single-Cas12a assay that isolates RNP T2 formation. In this configuration, either the gRNA, trigger DNA, or both remained blocked, generating a 2 × 2 matrix with four states: unblocked (i-a), trigger DNA-blocked (i-b), gRNA-blocked (ii-a), and dual-blocked (ii-b) (Fig. 2*E*). Fluorescence kinetics revealed progressive signal reduction as each blocking layer was introduced, with the lowest signal observed in the dual-blocked state (Fig. 2*F* and *SI Appendix*, Fig. S2 *D* and *E*). Blocking efficiencies (or signal reduction), calculated as the fluorescence ratio of the fully unblocked condition (i-a) to each blocked state at certain time points, demonstrated that scgRNA alone provided ~23.9-fold suppression at 10 min, whereas the Cascade probe alone yielded only ~1.1-fold suppression. Strikingly, dual-blocking achieved ~94.2-fold suppression, with the strongest effect at early timepoints (~106.1-fold at 5 min), suggesting efficient prevention of premature RNP formation that would otherwise trigger the positive-feedback reaction (*SI Appendix*, Fig. S1). This suppression exceeded the expected product of the individual blocking efficiencies, indicating a synergistic interaction between the orthogonal gRNA- and trigger-blocking pathways.

These single-Cas12a results using RNP T2 components show not only the advantage of combining scgRNA and the Cascade probe but also help us to understand why existing CRISPR autocatalytic systems often display substantial background leakage. When transitioning from the unblocked to trigger-blocked condition (i-a to i-b), signal persisted (Fig. 2*F* and *SI Appendix*, Fig. S2*D*) because the RNP can easily strand-invade the Cascade probe and partially unwind the duplex, thereby exposing the target regions of trigger DNA and enabling activation even in the blocked state (*SI Appendix*, Fig. S1*B*) (17, 18). Conversely, transitioning from unblocked to gRNA-blocked (i-a to ii-a) revealed that Cas12a can also invade scgRNA and form functional RNP despite inhibitory strands (*SI Appendix*, Fig. S1*A*). Surprisingly, even when both components were blocked (ii-b), signal gradually emerged over time (blue line, *SI Appendix*, Fig. S2*E*). If this background originates solely from unpaired or incompletely blocked DNA (thermodynamic respiration), providing excess complementary blockers should strongly suppress the signal. However, even increasing the blocker ratios (gRNA:iDNAs and trigger:bubble) from 1:1 up to 1:2 only modestly reduced leakage and did not fully eliminate it (*SI Appendix*, Fig. S2 *F* and *G*). This observation suggests that the background activity cannot be explained by equilibrium dynamics alone but instead reflects a kinetic bypass pathway in which Cas12a could actively invade and unwind apparently stable blocking structures, leading to residual activation despite strengthened thermodynamic pairing. A quantitative description of this leakage suppression trend as a function of blocker stoichiometry (x, y, z) and equilibrium parameters is provided in the *SI Appendix, Supplementary Note 2 Varying Complement Concentration*.

Finally, we verified that target-activated RNP T1 can cleave ssDNA bulges and release functional products (*SI Appendix*, Fig. S3). Incubation of the scgRNA or Cascade probe with the activated RNP T1 (detailed protocol in *SI Appendix*, Fig. S3*A*) generated trans-cleavage fragments (*SI Appendix*, Fig. S3 *B* and *D*). Increasing precleavage time led to progressively higher downstream signals in reporter assays (*SI Appendix*, Fig. S3 *C* and *E*), confirming that unblocked gRNA and trigger DNA produced by activated RNP T1 cause downstream activation of additional RNP. Together, these data validate the dual-blocking architecture, quantify its suppression capacity, and provide a potential mechanistic explanation for leakage in prior CRISPR autocatalytic systems which underscores the necessity of an orthogonal two-barrier strategy (Fig. 1*A*). This conceptual mechanism is further illustrated in Fig. 2*G*, where the dual-blocking architecture functions as an AND gate composed of two imperfect molecular switches, and the resulting suppression of background signal arises from the

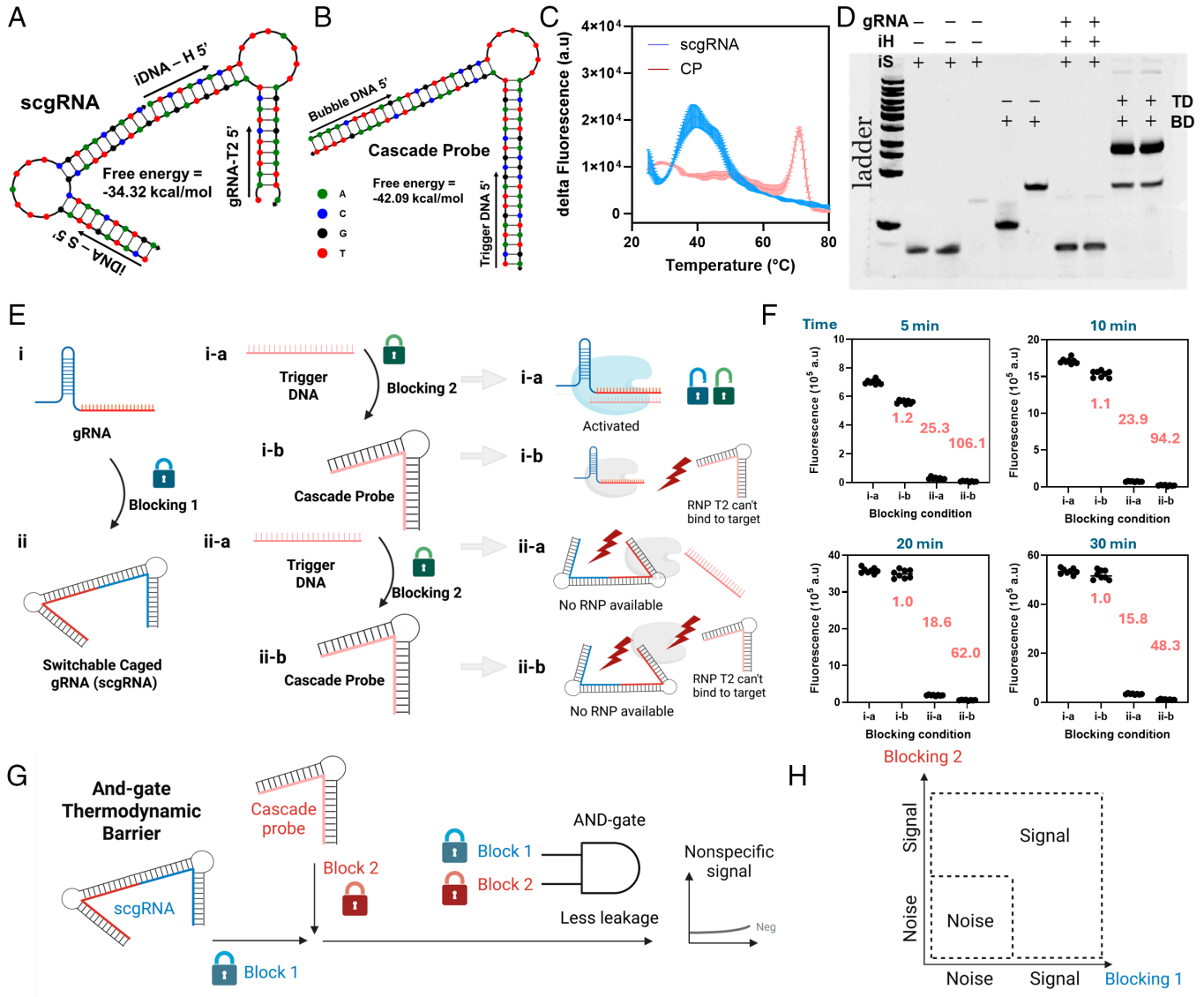


Fig. 2. Construction and baseline evaluation of dual-blocking components. (*A* and *B*) NUPACK-predicted secondary structures of scgRNA and the Cascade probe, with annotated 5′ starting points for gRNA-T2, inhibitor handle (iH), inhibitor spacer (iS), trigger DNA (TD), and bubble DNA (BD), along with their calculated free energies. (*C*) Melting-curve profiles of assembled scgRNA and Cascade probe. (*D*) Native PAGE analysis of scgRNA and Cascade probe alongside individual component strands. (*E*) A 2 × 2 single Cas12a reaction matrix was used to isolate RNP T2 formation and evaluate four precursor states: unblocked (i-a), trigger-blocked (i-b), gRNA-blocked (ii-a), and dual-blocked (ii-b). (*F*) Fluorescence signal at various time points of the four precursor states in the single-Cas12a assay. Signal reduction (fold), defined as the fluorescence ratio relative to the unblocked state, are shown in red for each time-point and condition. (*G*) Schematic illustration showing that dual-blocking operates as a AND gate, where scgRNA sequestration functions as the primary kinetic checkpoint followed by Cascade-probe activation. (*H*) Conceptual schematic showing that dual-blocking suppresses leakage multiplicatively (*SI Appendix, Supplementary Note 1*). While single blocking scales with $(1 - \alpha_1)$, dual-blocking requires simultaneous activity of both steps and scales as $(1 - \alpha_1)(1 - \alpha_2)$, thereby reducing background and stabilizing the OFF state. Data are presented as mean ± error (n = 3) in panel *C*, and as individual replicate traces (n = 8) in panel *F*.

multiplicative combination of the two blocking steps. Fig. 2*H* visualizes the dual-blocking design in a two-dimensional (2D) control space. In one-dimensional (1D) single-blocking systems, background noise is defined along a single axis, where leakage arises from imperfect blocking of one molecule. In contrast, in the 2D dual-blocking space, noise is confined to the intersection of two imperfect blocking events, corresponding to the product of the two independent constraints. As a result, the effective noise region is substantially reduced, leading to enhanced signal-to-noise ratio through multiplicative suppression (*SI Appendix, Supplementary Note 1*).

Engineering Cascade Probe Stability to Balance Dual-Blocking Contributions. While dual-blocking substantially reduced background compared to the single-blocking strategy (Fig. 2*F*), the two blocking modules did not contribute equally to leakage suppression. For example, the gRNA-blocking module (scgRNA) imposed a much stronger barrier (25.3-fold suppression at 5 min, Fig. 2*F*), whereas the trigger-blocking module (Cascade probe) offered only modest suppression in its initial configuration (1.2-fold suppression at 5 min, Fig. 2*F*), resulting in an imbalanced AND-gate behavior (Fig. 3*A*). Although the imbalance is not inherently detrimental, it indicates that the trigger-blocking pathway offers greater room for optimization compared to the gRNA-blocking module. To strengthen the trigger-blocking pathway, we systematically engineered Cascade probe designs by varying: i) bubble-DNA length for partially blocked Cascade probes, ii) the number of bulge units embedded in the bubble DNA, iii) placement of locked nucleic acids (LNAs) adjacent to bulges to enhance local stability (23, 24). We also iv) segmented the bubble DNA into two

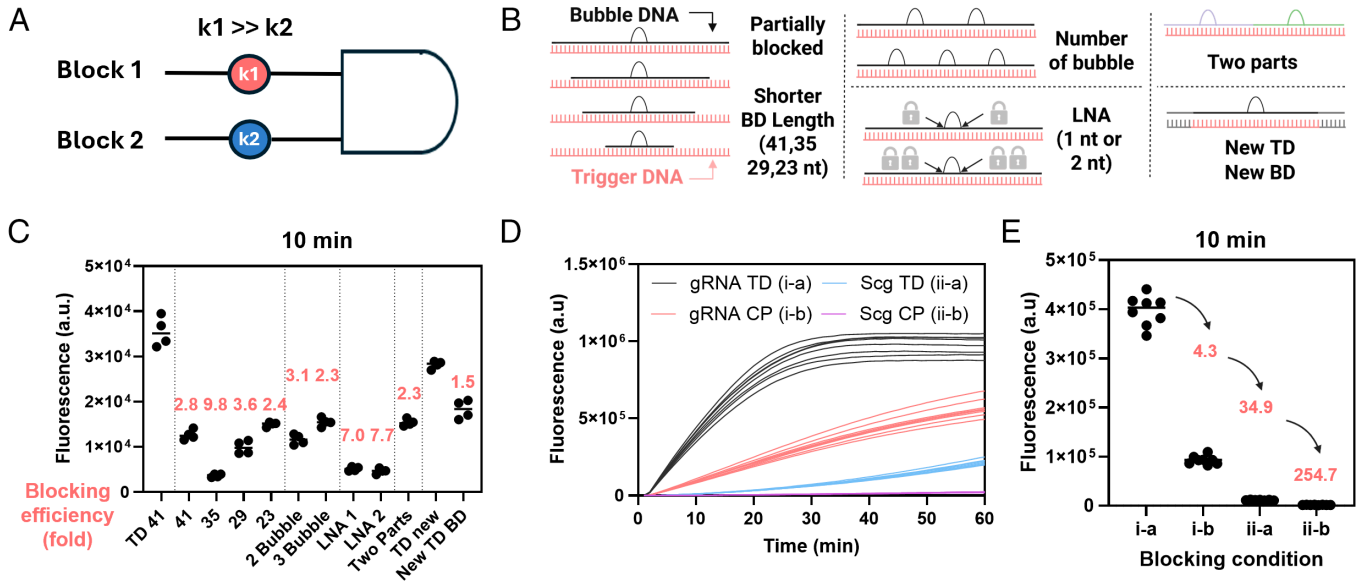


Fig. 3. Engineering Cascade probe stability to balance dual-blocking contributions. (*A*) Schematic illustrating the initial asymmetry between gRNA-blocking (scgRNA) and trigger-blocking (Cascade probe) pathways in the dual-blocking system. The scgRNA contributed a disproportionately stronger inhibition relative to the Cascade probe ($k^1 >> k^2$), resulting in an unbalanced AND-gate behavior. (*B*) Cascade probe variants tested, including designs with altered bubble-DNA length, bulge count, LNA placement, duplex segmentation, and trigger-DNA sequence. (*C*) Single-Cas12a assay comparing fluorescence profiles at t = 10 min using gRNA with either unblocked trigger DNA ("TD41" or "TD-new") or Cascade probe variants. Bubble-DNA lengths (41, 35, 29, and 23 nt) represent designs shortened in 6-nt increments (excluding bulges); "2-bubble" and "3-bubble" indicate the number of bulge units; "LNA-1" and "LNA-2" indicate incorporation of one or two LNAs beneath the bulge; "two-parts" indicates division of the bubble-DNA into two segments; TD-new denotes an alternative trigger-DNA sequence; and "new-TD-BD" is the corresponding Cascade probe for that trigger. Blocking efficiencies are shown in red. For example, the TD41 signal divided by the CP41 signal yields a blocking efficiency of 2.8. (*D*) Representative 2 × 2 single-Cas12a kinetic traces using the LNA-1 probe variant. (*E*) End-point signal and calculated blocking efficiencies using the LNA-1 probe. Data are shown with individual replicates (n = 4 for panel *C*, and n = 8 for panels *D* and *E*).

parts, analogous to scgRNA's iDNAs (9) and v) varied the trigger-DNA sequence (Fig. 3*B* and *SI Appendix*, Figs. S4 and S5).

Single-Cas12a measurements using gRNA together with either trigger DNA (TD41) or various Cascade probes (corresponding to the i-a and i-b conditions in Fig. 2*F*) showed that Cascade probes containing a 35-nt bubble DNA (BD35) or LNA-modified bulges achieved the strongest blocking, with 7.0 to 9.8-fold suppression relative to unblocked TD41 controls (Fig. 3*C*). Representative kinetic profiles using the LNA-optimized Cascade probe confirmed that the contribution of the two blocking modules became more balanced (Fig. 3*D*). In the unblocked condition (i-a), signal rose rapidly as expected. When only the Cascade module was blocked (i-b), suppression reached 4.3-fold, whereas scgRNA-only blocking (ii-a) yielded 34.9-fold suppression at 10 min (Fig. 3*E*). Dual-blocking (ii-b) resulted in the strongest suppression, giving ~254.7-fold signal reduction. This combined effect exceeded the expected product of the individual-blocking efficiencies by approximately 1.7-fold, indicating a measurable synergistic interaction between the two blocking modules. Full datasets at 10, 20, and 30 min are provided in *SI Appendix*, Figs. S6 and S7. These results show that increasing the blocking efficiency of the Cascade probe narrows the performance gap between the two blocking pathways and produces a more balanced AND-gate response. However, blocking efficiency alone does not always correlate with robust switching performance, as signal suppression may also occur. Thus, full assay characterization is required.

Regardless of blocking-probe enhancements, scgRNA blocking remained the dominant contributor to suppression, even under optimized probe designs. This behavior reflects the intrinsic reaction order in which Cas12a must first bind gRNA to form the initial RNP complex before engaging any trigger substrate (25, 26). Accordingly, gRNA sequestration among the two BNA components imposes the primary kinetic checkpoint, yielding a sequential AND-gate architecture initiated by scgRNA (*SI Appendix*, Fig. S8).

Enabling Ultrasensitive CRISPR Detection by Integrating Dual-Blocking into the Full Cascade Workflow. Next, we implemented the dual-blocking architecture within a complete CRISPR-Cascade assay. To enable systematic characterization of the assay, we first defined a consistent reference configuration. Two sample inputs were used throughout: MRSA genomic DNA (10^4 copies/μL) as the positive control and a no-target negative control, both in nuclease-free water. For SNR calculations, these positive and negative samples were measured in parallel under identical conditions. The concentrations of the two blocking modules, scgRNA and Cascade probe, were fixed at 10 nM each (*SI Appendix*, Fig. S9), and the RNP T1:RNP T2 ratio was set to 1:3. CP-41 was selected as the reference Cascade probe to provide a baseline performance. This baseline served as the reference condition for all subsequent optimization and benchmarking studies, unless otherwise specified for configurations yielding superior performance. Under this condition, we compared the signal-to-noise ratio (SNR) between positive and negative samples at t = 10 min, establishing a quantitative reference point for subsequent performance improvements.

We first optimized the reaction sequence. Cas12a was first pre-complexed with MRSA-targeting gRNA (preincubation, 5 min; Fig. 4 *A*, *i*), followed by target DNA activation (preactivation, 5 min; Fig. 4 *A*, *ii*). The activated RNP T1 complex was then introduced to the dual-blocked T2 components (Fig. 4 *A*, *iii*), enabling RNP T1 to turn on the autocatalytic switch and RNP T2 to drive positive-feedback amplification (Fig. 4*B*). To identify the most effective reaction workflow, we evaluated three configurations (Fig. 4*C*): i) preactivation only, in which Cas12a, gRNA, and target DNA were introduced simultaneously without prior RNP assembly ("i ii combined"); ii) sequential preincubation followed by preactivation, allowing RNP T1 formation before target engagement ("Final Protocol"); and iii) one pot assembly, in which all components, including the T2 module, were combined at the

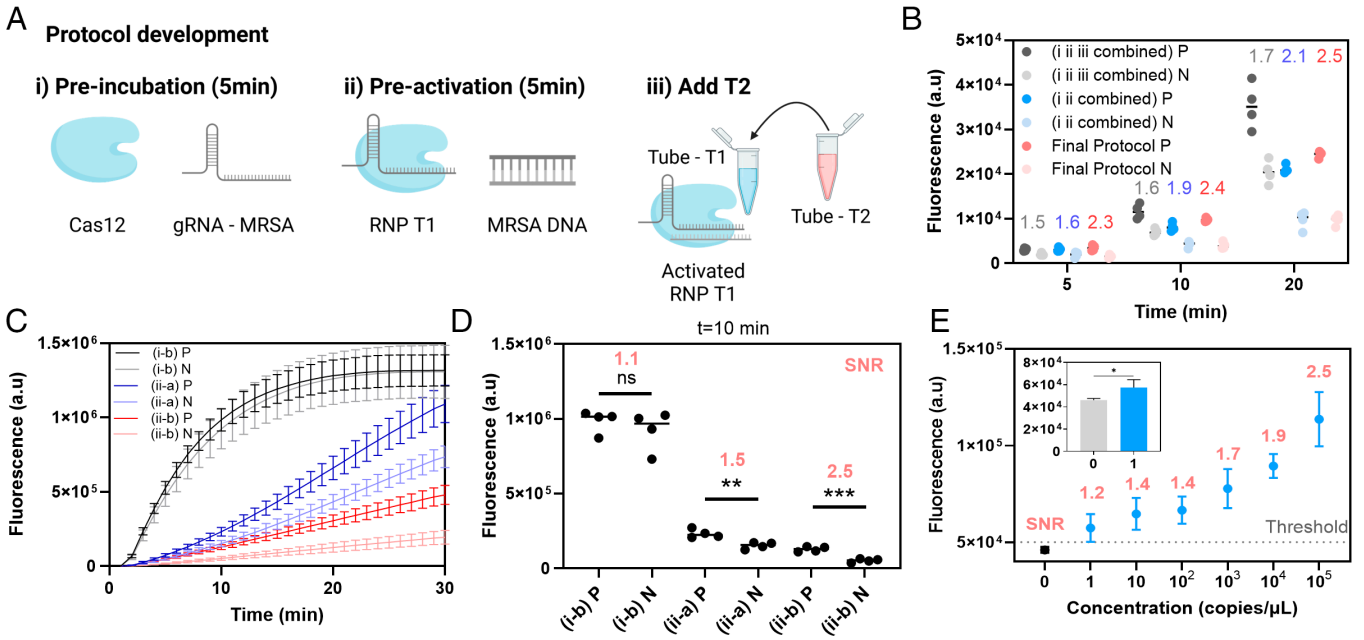


Fig. 4. Integrating dual-blocking into the full CRISPR-Cascade workflow. (*A*) Schematic of the reaction sequence: i) Cas12a preincubation with gRNA-MRSA forming RNP complex, ii) target DNA preactivation by adding sample, and iii) introduction of the dual-blocked RNP T2 components into the activated RNP T1. (*B*) Comparison of three reaction workflows: preactivation without preincubation [(i ii combined), blue], sequential preincubation followed by preactivation (Final Protocol, red), and one pot assembly of all components [(i ii iii combined), gray]. End point fluorescence is shown at 5, 10, and 20 min. Positive samples, denoted as P (10^4 copies per microliter MRSA genomic DNA), are shown in darker colors, and negative samples, denoted as N (no template), are shown in lighter colors. The SNR for each case is displayed numerically in the corresponding color. (*C*) Kinetic traces for positive samples (P, shown in darker colors) and negative samples (N, shown in lighter colors) under dual-blocking and single blocking configurations. The condition using scgRNA with trigger DNA (scg TD, blue) represents single blocking 1, the condition using gRNA with Cascade probe (gRNA CP, red) represents single blocking 2, and the condition using both scgRNA and Cascade probe (scg CP, gray) represents dual-blocking. (*D*) End-point signal and SNR analysis at 10 min demonstrates that dual-blocking improves discrimination by disproportionately suppressing leakage. (*E*) Serial dilution of MRSA genomic DNA showing end-point readout at 10 min from single copy to 10^4 copies per microliter. The signal-to-noise ratio (SNR) was calculated by dividing each concentration by the corresponding negative sample and is displayed in red. The inset shows statistical analysis comparing negative and lowest positive (1 copy per microliter) samples from the full calibration. Statistical analysis was performed using a two tailed unpaired *t* test; the asterisk indicates *P* less than 0.05. Data are presented with individual replicates (n = 4 for panels *B* and *D*), and with mean and SD (n = 4 for panel *C* and n = 5 for panel *E*).

outset with no precomplex formation ("i ii iii combined"). The sequential protocol (ii) integrating preincubation and preactivation produced the strongest signal separation between positive and negative samples, demonstrating that staged RNP assembly and activation enhances controlled engagement of the T2 autocatalytic module.

Using this optimized workflow, we then evaluated assay performance under varied molecular designs and reaction conditions. First, we screened different Cascade probe variants. Surprisingly, CP29, rather than CP35 or the LNA-modified probe, yielded the highest SNR (1.87; *SI Appendix*, Fig. S10), demonstrating that maximal blocking efficiency (Fig. 3*C*) does not necessarily translate to optimal switching fidelity or assay accuracy. This is because blocking strength reduces background but does not dictate how quickly RNP T1 can cleave the bulge and amplify signal, making SNR dependent on the balance between kinetic activation and background suppression rather than blocking efficiency alone. Guided by this result, we used CP-29 for subsequent optimization. We next evaluated buffer composition (*SI Appendix*, Fig. S11*A*) and RNP T1:T2 ratios (*SI Appendix*, Fig. S11 *B* and *C*). Together, these analyses identified the optimal configuration as 10 nM scgRNA, 10 nM Cascade probe, NEB Buffer 2.1, a 1:3 RNP T1:T2 ratio (corresponding to a final concentration of 6 nM for both scgRNA and Cascade probe), and CP-29 as the standard Cascade probe for subsequent experiments.

We next benchmarked the dual-blocking circuit against each single-blocking configuration (Fig. 4 *C* and *D*). All reaction conditions were identical across groups, except that one blocking element (scgRNA or Cascade probe) was replaced with its unblocked counterpart (gRNA or trigger DNA) at the same concentration to ensure a fair comparison. Dual-blocking markedly suppressed background, reducing leakage by 2.94-fold relative to scgRNA-only blocking, and by 17.81-fold relative to trigger-DNA blocking (*SI Appendix*, Fig. S12*A*). This is consistent with leakage trends observed in the single-Cas12a characterization of RNP T2 (Figs. 2*F* and 3*E*). While positive signals also decreased (7.66-fold and 1.80-fold respectively, *SI Appendix*, Fig. S12*B*), the overall signal-to-noise ratio (SNR) improved (*SI Appendix*, Fig. S12 *C* and *D*). As a result, scgRNA-only blocking yielded a modest SNR of 1.5 at 10 min, and trigger-DNA-only blocking produced a near-baseline SNR of 1.1, whereas the dual-blocking architecture achieved a substantially higher SNR (2.5 at 10 min; *SI Appendix*, Fig. S12*C*). These data indicate that while the dual-blocking strategy attenuates both signal and noise, the suppression of noise outpaces the signal suppression and results in enhanced assay performance. For comparison, a single-Cas12a reaction lacking the Cascade signal amplification detected only ~10 pM targets (*SI Appendix*, Fig. S13), illustrating the intrinsic sensitivity limit without positive feedback, and underscoring that autocatalytic amplification is essential for highly sensitive detection (27, 28).

Finally, 10-fold serial dilutions in nuclease-free water of MRSA genomic DNA revealed detection down to the single-copy regime, with SNR values between 1.2 and 2.5 across replicates (Fig. 4*E*). Full calibration curves, including titration behavior across the dilution series, are provided in *SI Appendix*, Fig. S14. For the

one-pot assembly reaction, the calibration curve showed poor discrimination in fluorescence over time between concentrations below 10^3 copies/μL (*SI Appendix*, Fig. S15), highlighting the importance of supplying RNP T1 separately from the autocatalytic RNP T2 layer to fully preserve sensitivity. Together, these results establish dual-blocking as an effective strategy that not only suppresses spontaneous leakage but also enables attomolar-level detection capability in a self-amplifying CRISPR system.

Eliminating Residual Leakage by a Sacrificial Guide RNA Decoy. Although dual-blocking substantially reduced leakage and improved signal discrimination (Fig. 4*D*), residual background activity remained detectable. To further suppress unintended activation, we implemented a simple competitive strategy in which a large molar excess of free gRNA T1 (up to tens of micromolar) was supplied as a decoy to outcompete premature RNP T2 formation (Fig. 5*A*). Because gRNA is not a significant trans-cleavage target on its own, it can be supplied in large excess as a decoy without interfering with Cas12a activity or overall reaction kinetics (29). Because the decoy is present in large excess of any unblocked scgRNA exposed by the respiratory effect, it should outcompete the noise-generating species, preventing unwanted RNP activation. Once the RNP is cleaved as a result of target activation, the increasing concentration of scgRNA unblocked via cleavage is able to compete with the decoy and cause signal amplification. This strategy effectively reduces unintended activation driven by scgRNA unwinding (*SI Appendix*, Figs. S1*A* and S16).

Critically, the decoy strategy selectively suppressed negative control leakage without compromising true signals. When only the T2 module was present without RNP T1, strong spontaneous activation occurred (black line, Fig. 5*B*). In the full Cascade, adding increasing amounts of decoy gRNA progressively reduced background amplification under negative-control conditions (Fig. 5*B*), while positive reactions (10^4 copies/μL MRSA DNA) remained stable at ~3 to 4 × 10^5 a.u. across all decoy concentrations (Fig. 5*C*). As a result, the SNR increased from ~1.0 to ~11.1 as the decoy concentration was raised from 500 nM to 50 μM. Unlike the addition of background DNA, which reduces both positive and negative signals by diverting Cas12a trans-cleavage activity (13), the gRNA-decoy operates through a trans-cleavage-independent mechanism: it selectively sequesters free Cas12a before unintended RNP formation, thereby eliminating leakage without significantly

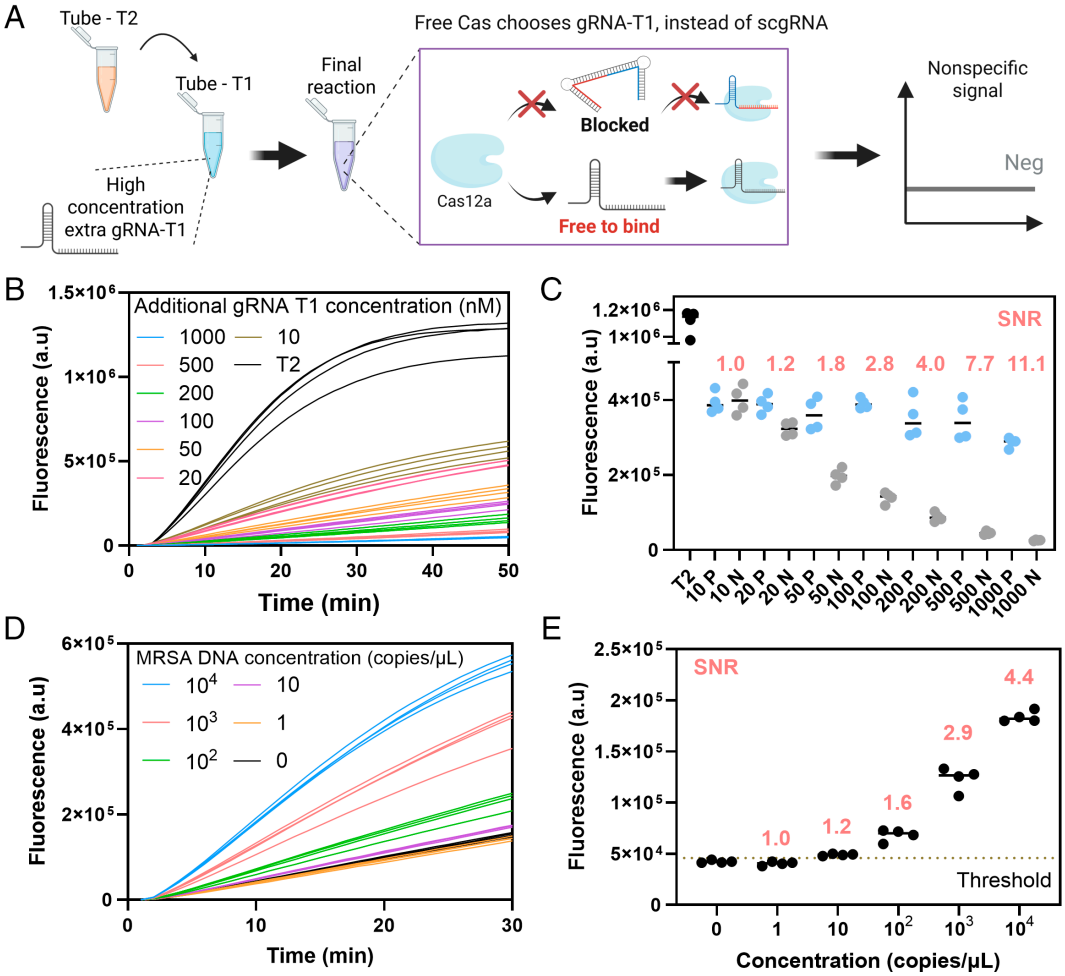


Fig. 5. Suppressing residual leakage using a competitive gRNA decoy strategy. (*A*) Schematic illustrating the decoy concept. Extra gRNA T1 is supplied in T1 tube, remaining unbound until mixed with T2 components. Free Cas12a in the T2 tube preferentially binds the unblocked decoy gRNA T1 rather than the blocked scgRNA. This competitive binding prevents premature RNP T2 formation driven by scgRNA unwinding, resulting in reduced nonspecific signal. (*B*) Negative control fluorescence traces with increasing concentrations of decoy gRNA T1, showing progressive suppression of background activation. (*C*) End point fluorescence at 30 min for positive (10^4 copies per microliter MRSA genomic DNA) and negative (no template) are shown at corresponding decoy concentrations (nM), showing minimal effect on true signal generation. The SNR is displayed above each condition with purple color. (*D*) Detection of MRSA genomic DNA at varying concentrations from 10^4 to 1 copies per microliter with decoy gRNA protocol. (*E*) Endpoint signal and signal to noise ratio at 10 min across MRSA dilutions. Data are shown with individual well replicates (n = 4 for all panels).

affecting reaction kinetics. In comparison, adding 3 ng/μL human genomic DNA reduced both positive and negative fluorescence (*SI Appendix*, Fig. S17*A*), yielding only a modest SNR improvement (~2.58 to ~3.19; *SI Appendix*, Fig. S17*B*).

The effect of the decoy gRNA was sequence independent. Unrelated gRNA sequences used previously by our group produced similar suppression trends (*SI Appendix*, Fig. S18), indicating that the benefit arises from competitive Cas12a binding rather than target-dependent interactions. Extended monitoring showed that the leakage signal remained at baseline for several hours (*SI Appendix*, Fig. S19), reminiscent of PCR reactions, in which true negatives remain flat. Combining multiple MRSA-targeting guides further enhanced the signal output (9.8 to 12.2; *SI Appendix*, Fig. S20), consistent with prior reports of multiguide synergy in CRISPR systems (30). Based on these results, we used four MRSA-targeting decoy gRNAs (31–33), each at 5 μM, and evaluated quantitative performance across MRSA genomic DNA concentrations from 10^4 to 1 copies/μL (Fig. 5 *D* and *E*). With the decoy strategy, SNR at 10^4 copies/μL improved from ~1.9 (Fig. 4*E*) to ~4.4 (Fig. 5*D*), while ultra-low inputs remained detectable but with slightly reduced sensitivity, slightly raising the practical detection limit from 1 copy per μL to about 10 copies per μL (SNR ≈ 1.2).

Analysis of Blood Sample with Dual-Blocking. Last, we evaluated the performance of our dual-blocking CRISPR-Cascade assay using mock clinical samples spiked with MRSA pathogens in whole blood. Whole blood was inoculated with MRSA at 10-fold serial dilutions to simulate clinically relevant pathogen loads, followed by standard lysis and DNA extraction using commercial kits (Fig. 5*A*). The extracted nucleic acids were then tested using our optimized dual-blocking configuration, which combines CP29, a decoy gRNA-T1, and a four-guide MRSA gRNA-T1 pool.

The total time-to-result was 40 min, consisting of 10 min for thermal lysis, 10 min for extraction and purification, 5 min of preincubation of RNP T1, 5 min of preactivation with sample, and a 10-min dual-blocking reaction and readout step (Fig. 6*A*). Across biological replicates, our assay successfully detected MRSA in spiked blood samples down to 200 CFU per 200 μL (Fig. 6*B*), yielding SNR values ranging from 1.3 to 12.9 for positive and 0.96 to 1.29 for negative value (Fig. 6*C*). Using a receiver operating characteristic (ROC) curve, threshold SNR was established as 1.293, the assay correctly classified positive and negative samples with a 100 percent sensitivity and specificity, clearly separating true positives from true negatives.

The observed sensitivity was limited by DNA loss during column-based purification, which reduces assay input efficiency at low pathogen concentrations. In particular, samples spiked with 2 and 20 CFU per 200 μL were classified as negative in the PCR analysis (*SI Appendix*, Fig. S21), indicating that the reduced sensitivity primarily arose from extraction-related sample loss rather than from any limitation of the dual-blocking assay itself. Thus, coupling this autocatalytic CRISPR system with loss-free sample-handling strategies, such as our previously reported biphasic preparation protocol, may enable recovery of these ultra-low targets and further enhance real-world performance (34–37). Taken together, these findings show that the dual-blocking CRISPR-Cascade integrates robustly with routine clinical sample-processing methods, delivering rapid (~40 min) and sensitive MRSA detection from purified whole-blood samples.

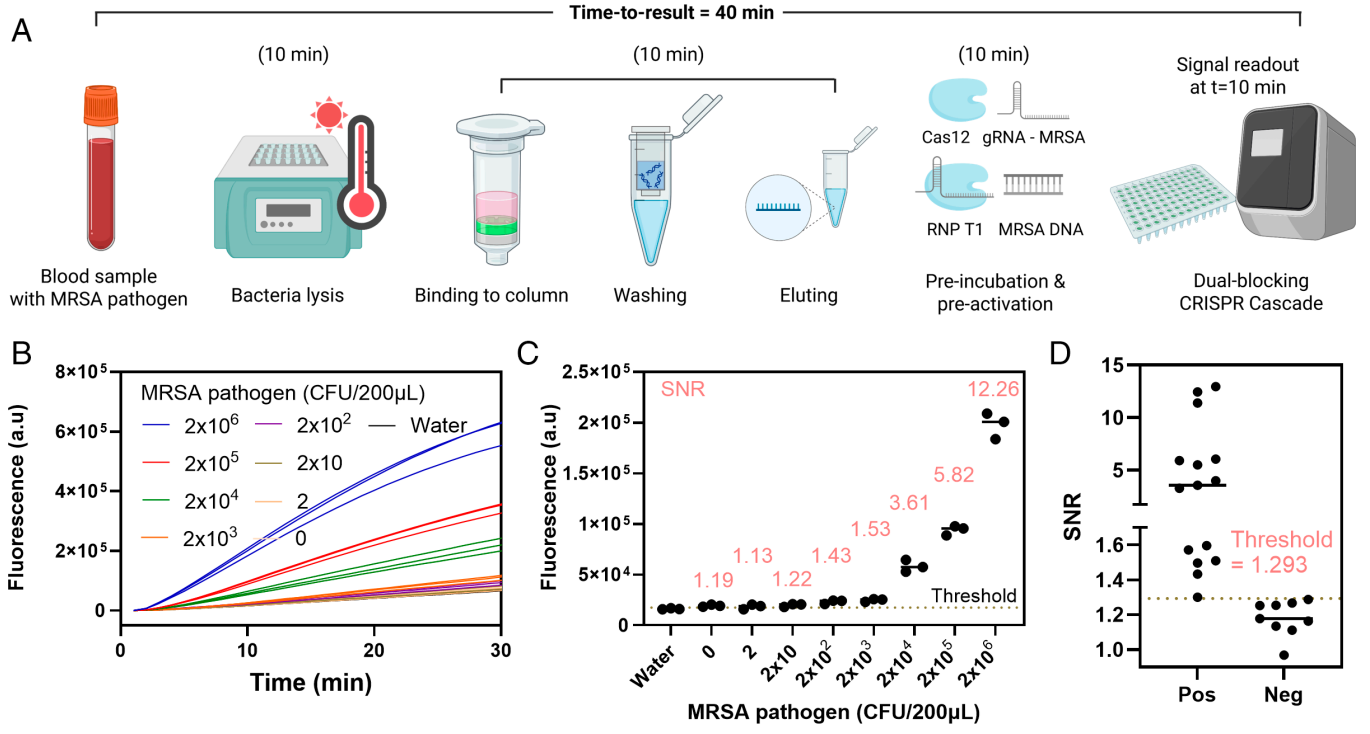


Fig. 6. Evaluation of the dual-blocking CRISPR-Cascade assay using whole-blood samples spiked with MRSA. (*A*) Workflow for mock clinical testing with MRSA-spiked whole blood, involving thermal lysis, column-based DNA extraction, and dual-blocking CRISPR-Cascade detection, completed within 40 min. (*B*) Time-resolved fluorescence profiles of the dual-blocking CRISPR-Cascade reactions over 30 min across varying MRSA concentrations, showing progressively increased signal intensity with higher pathogen loads. (*C*) End-point fluorescence and corresponding signal-to-noise ratio (SNR) values measured at 10 min, with SNR values highlighted in red. (*D*) Distribution of signal-to-noise ratio (SNR) values for positive and negative samples. Receiver operating characteristic (ROC) analysis established a threshold SNR of 1.293. Data are shown with individual well replicates (n = 3).

Discussion

We demonstrate that dual-blocking both gRNA and trigger DNA provides two orthogonal kinetic gates, sharply reducing background activation (3 to 18-fold) while preserving attomolar sensitivity. This strategy substantially reduces nonspecific activation in autocatalytic CRISPR reactions by imposing two sequential kinetic thresholds, thereby limiting spontaneous RNP formation and boosting signal discrimination (Fig. 4*D*). These findings expand the design principles for leakage-suppressed CRISPR circuits, highlighting the importance of coordinated control over both gRNA and trigger-DNA inputs in self-amplifying reactions.

The dual-blocking architecture functions as a molecular analogue of split-activator logic. Whereas previous split activators divide a single activator substrate into two fragments that require colocalization (38, 39), our design applies a similar principle across two orthogonal biochemical species: the guide RNA and trigger DNA. Looking forward, this architecture could be further generalized. For example, splitting the trigger DNA into two fragments, each masked by its own bubble-DNA, would produce a triple-blocking configuration. Three-layer gating could further enhance kinetic insulation that further suppresses unintended RNP formation. Systematically evaluating higher-order gating architecture represents an intriguing direction for minimizing nonspecific signals in autocatalytic systems.

Despite strong suppression in the dual-blocking configuration, residual leakage was still observed. This background likely arises from enzyme-driven strand invasion events: Cas12a can unwind scgRNA to form functional RNPs, and active RNPs can strand-invade Cascade probes (17, 18), gradually exposing trigger sequences over time (*SI Appendix*, Fig. S1). These leakage pathways appear difficult to eliminate solely through thermodynamic stabilization, suggesting that autocatalytic CRISPR circuits reach a biochemical ceiling in leakage suppression when relying only on nucleic-acid-based gates. Notably, introducing a large molar excess of sacrificial gRNA-T1 created a kinetic sink for Cas12a, diverting it away from blocked precursors and nearly abolishing background activation. This observation points to hybrid gating strategies combining dual nucleic-acid caging and saturating enzyme competition as a promising direction for approaching truly zero-leakage behavior. Looking ahead, it will be valuable to develop generalizable RNP T2 components paired with sequence-agnostic decoy guides that function independently of target identity. Strategies such as truncated guides or spacer-only RNAs lacking scaffold domains may offer a path toward universal decoy designs capable of suppressing leakage across diverse targets through improved nuclease specificity (40, 41).

Our architecture also streamlines point-of-care operation. Although a two-step configuration was used here to maximize performance, this design introduces a minor contamination risk similar to but less severe than conventional two-pot preamplification workflows. This limitation can be readily mitigated through strategies such as closed tube integration, physical barriers, or lyophilized reagents, which would enable a true one pot implementation without compromising sensitivity (42). To be specific, because Cas12a and gRNA can be preassembled into RNP T1 and lyophilized directly, the preincubation step can be eliminated entirely (2, 43, 44). RNP T2 precursors can likewise be preformulated, enabling a simple workflow in which both modules are rehydrated, mixed with the sample, and incubated isothermally. Future work could focus on optimizing lyophilization and stabilization chemistries to support robust storage, transport, and deployment in resource-limited settings.

An important consideration in scaling this technology is the increased design space associated with dual-blocking. Compared to single-blocking systems, dual-blocking introduces multiple tunable components, including the stoichiometry of trigger DNA to bubble DNA and ratios of RNP T1 to RNP T2 precursors. These variables offer opportunities to tailor dynamic range, kinetics, and specificity but also introduce optimization complexity (28). To systematically navigate this parameter space, reaction-kinetic modeling and computational design frameworks will be valuable (45, 46). Our group recently established a quantitative kinetic modeling framework for target amplification-free CRISPR–Cas autocatalytic reactions, enabling analysis of autocatalytic nucleic acid (ANA) stability, background ssDNA inhibition, and reagent-dependent assay optimization in silico (47). In-silico simulations that incorporate strand-exchange kinetics, R-loop formation, and enzyme–substrate competition could guide experimental design by predicting conditions that minimize leakage while maintaining amplification gain (48, 49). Coupling such predictive modeling with targeted experimental screening will accelerate parameter identification and provide a rational foundation for optimizing multilayer CRISPR autocatalytic circuits. However, current models are limited by incomplete understanding of the precise secondary structures that undergo strand invasion, making it challenging to fully capture unwinding dynamics in silico. Continued experimental characterization of blocked state conformations will therefore be critical for improving model accuracy and guiding next generation circuit design. Another significant limitation lies in accurately modeling RNA–DNA duplex formation (50–52). Current computational frameworks are primarily optimized for DNA–DNA or RNA–RNA interactions, and the hybridization thermodynamics and secondary structure prediction for RNA–DNA hybrids remain poorly parameterized. The lack of experimentally validated energy models and kinetic constants for such heteroduplexes makes in-silico integration of RNA strands challenging. Developing improved hybrid thermodynamic models will be crucial for advancing predictive design of mixed nucleic acid systems in CRISPR autocatalytic circuits. Ultimately, integrating computational and empirical approaches will be essential for refining next-generation self-amplifying CRISPR platforms and expanding their translational readiness.

Overall, dual-blocking establishes a generalizable blueprint for constructing self-amplifying CRISPR systems with PCR-like binary discrimination, yet without thermal cycling. By combining orthogonal gating, sacrificial competitor strategies, and systematic optimization, our approach addresses fundamental leakage challenges that have limited previous self-amplifying CRISPR assays. Our design improves practical specificity by maintaining a completely flat baseline in the absence of target, thereby enabling clear on–off switching behavior.

Conclusion

This work establishes a dual-blocking autocatalytic CRISPR-Cascade architecture that addresses the intrinsic leakage mechanisms that have limited previous amplification-free CRISPR systems. By independently caging the guide RNA and the trigger DNA, the system introduces two orthogonal kinetic barriers that markedly suppress spontaneous RNP formation, while preserving rapid detection and attomolar sensitivity. Incorporation of a sacrificial guide RNA decoy adds a third AND gate component by acting as a kinetic sink for Cas12a, further reducing unintended activation and driving the baseline toward PCR-like flat behavior in the absence of target. Together, these multilayer strategies enable robust MRSA pathogen detection from purified whole blood within 40 min and achieve complete classification accuracy in spiked samples, demonstrating practical diagnostic utility. More

broadly, the modularity and generalizability of the dual-blocking design provide a framework for constructing next generation self-amplifying CRISPR circuits with reduced background noise and reliable AND gate switching suitable for diverse applications in molecular sensing and point of care diagnostics.

Materials and Methods

Reagents. PBS buffer (21040CV) was obtained from Corning. 10x TBE buffer (B52), UltraPure™ 1 M Tris-HCl Buffer (15567027)-pH 7.5, 5 M NaCl (2802039), and RNase-free water (AM9760G) were purchased from Thermofisher Scientific. 1X TE-pH 8.0, NEB low molecular weight DNA ladder (N3233S), Magnesium Chloride (MgCl2, B9021S), Murine RNase Inhibitor (M0314L), and NEBuffer™ r2.1 (5 mL, B6002S) solution were purchased from New England Biolabs (NEB). Alt-R™ LbCas12a (Cpf1) Ultra and all nucleic acid sequences were synthesized and obtained from Integrated DNA Technologies (IDT).

Pathogens and DNA Sequences. The synthetic MRSA DNA fragment was synthesized by IDT and dissolved in TE buffer. Genomic DNA from the MRSA strain HFH-30106 (NR-10320) was procured from BEI Resources (Manassas, VA), aliquoted to the required concentrations and volumes, and stored at −80 °C until use. For bacterial culture experiments, MRSA strain HFH-30106 (NR-10192) was likewise obtained from BEI Resources.

Switchable Caged Guide RNA and Cascade Probe Design and Sequences. The DNA and RNA oligonucleotides (detailed in *SI Appendix*, Table S1) were obtained as lyophilized format and subsequently reconstituted in Tris-EDTA (TE) buffer. 1 μM Cascade probes were prepared by hybridization the two complementary oligomers at the molar ratio of 1:1.5 of (trigger DNA:bubble DNA) at 95 °C for 4 min in annealing buffer [20 mM tris-HCl (pH 7.5), 50 mM NaCl, and 10 mM $MgCl_2$], followed by gradient cooling to 25 °C at a rate of 0.1 °C/s. 1 μM switchable caged guide RNA (scgRNA) solutions were also generated by the hybridization of the gRNA (gRNA T2), inhibitor-handle (iH) DNA, and inhibitor-spacer (iS) DNA using the same annealing procedure with the molar ratio of 1:1.2:1.2. The concentration of CP and scgRNA specified in the text refers to the concentration of the used gRNA and TD. All scgRNAs and CPs were prepared, aliquoted, and stored at −20 °C until use. Secondary-structure predictions for BNAs (i.e., CP and scgRNA constructs) were performed using NUPACK software under ionic conditions of 50 mM Na^+ and 10 mM Mg^{2+} at 37 °C. Because NUPACK does not support hybrid secondary-structure prediction between RNA and DNA strands within a single complex, the RNA guide sequences (gRNA) were converted to their DNA equivalents prior to simulation. This substitution preserves the base-pairing pattern and thermodynamic characteristics of the nucleic acid structures, allowing approximate estimation of the hybridization behavior and folding energy landscapes of the designed scgRNA complexes. For melting curve analysis, 1× Evagreen (Biotium) was added to each sample with the ratio of 9:1 (Evagreen:sample). Then, the melting curve was recorded using a QuantStudio3 (Applied Biosystems) instrument with a controlled temperature ramp rate of 0.1 °C/s.

Single CRISPR Cas12a Assay. The following protocol was applied to all single-Cas12a experiments, including the 2 × 2 matrix characterization shown in Figs. 2*F* and 3 *C*–*E*. In this format, each reaction consisted of one Cas12a enzyme complexed with a corresponding guide RNA and the target nucleic acid, which could be either in blocked or unblocked form. Specifically, the i-a condition in Fig. 2*F* represents the reaction containing gRNA-T2 and trigger DNA, while the i-b condition represents gRNA-T2 with the Cascade probe, where the target DNA is replaced with its blocked form. The ii-a condition corresponds to scgRNA with trigger DNA, and the ii-b condition to scgRNA with the Cascade probe, where both the gRNA and target are in blocked states. All single-Cas12a reactions were preincubated for 20 min at 37 °C with 10 nM LbCas12a, 10 nM gRNA, 0.4 U μL^{-1} Murine RNase Inhibitor, 500 nM fluorescent ssDNA reporter, 1× NEB buffer, and 2.5 mM $MgCl_2$. After preincubation, 9 μL of the reaction mixture was combined with 2 μL of the sample containing varying concentrations of target nucleic acids. The reaction was conducted on a QuantStudio3 real-time fluorescence reader, and fluorescence intensities were recorded every minute. Fluorescence data were normalized by subtracting the initial (0 min) fluorescence signal, and the signal-to-noise ratio was calculated by dividing the fluorescence signal of the positive group by that of the negative control at the time point of interest, in which RNase-free water served as the sample. The same conditions were used for RNP T2-only characterization experiments, except that RNP T1 was replaced by RNP T2 and the target molecules were substituted with the trigger DNA or Cascade probe.

High-Resolution Nondenaturing Polyacrylamide Gel Electrophoresis (PAGE) Assays. High-resolution nondenaturing polyacrylamide gel electrophoresis (PAGE) experiments were prepared with 15% polyacrylamide in 10× TBE (89 mM Tris, 89 mM boric acid, 2 mM EDTA). Gel solution was prepared by mixing 3.75 mL Biorad 40% Acrylamide/Bis Solution, 5.25 mL degassed water, 1 mL 10× TBE (ThermoFisher, 161-0733), 50 μL APS (1610700, 10% w/v solution), and 5 μL TEMED (1610800). NEB Low Molecular Weight Ladder (N3233S) was used as the DNA standard. The trans-cleavage activity of RNP T1 on scgRNA and Cascade probes was evaluated using nondenaturing polyacrylamide gel electrophoresis (PAGE). Cleavage reactions were quenched by transferring to ice, adding 2 μL of loading dye (with a ratio of 8 μl of RNP T1 solution to 2 μL of loading dye) and immediately loaded into the designated wells of the 15% acrylamide gel. Electrophoresis was carried out at room temperature under a constant voltage of 130 V for 3 to 4 h. Following electrophoresis, gels were stained with ThermoFisher SYBR 1 gel stain (S7563) prepared at a ratio of 5 μL 10× SYBR to 50 μL 1× TBE buffer, and gently agitated at 150 rpm in the dark for 40 min. Gels were imaged using a Bio-Rad gel documentation system.

CRISPR-Cascade Assay. For the dual-blocking Cascade assay, the RNP T1 complex, consisting of 10 nM LbCas12a, 10 nM target specific gRNA, 2.5 mM $MgCl_2$, and 1× NEB 2.1 buffer, was preincubated at 37 °C for 5 min to allow RNP formation. The preassembled RNP T1 was then activated by mixing with pathogen genomic DNA at 37 °C for 5 min in a 1:1 volume ratio of RNP T1 to sample. Separately, RNP T2 complexes were prepared with 10 nM LbCas12a, 0.4 U/μL Murine RNase Inhibitor, 500 nM DNA fluorescent probe, 1× NEBuffer™ r2.1, and an additional 2.5 mM $MgCl_2$, and stored at 4 °C until use. After activation of RNP T1, RNP T2 was supplemented with 10 nM scgRNA and 10 nM Cascade probe to complete the reaction mixture. The completed RNP T2 complex was then combined with the activated RNP T1 at a 3:1 volume ratio. For assay development and performance characterization, the concentrations of RNP T1 and RNP T2 were kept constant, while their mixing ratio was systematically varied from 1:1 to 1:48. Reactions were performed on a QuantStudio3 instrument with fluorescence signals recorded at 1-min intervals. Fluorescence readings were baseline-corrected by subtracting the initial (0-min) value, and the signal-to-noise ratio was determined by dividing the fluorescence intensity of the positive sample by that of the negative control. For each single blocking Cascade assay in Fig. 4 *C* and *D*, all groups were tested under identical reaction conditions, with the only difference being that one blocking component (either the scgRNA or Cascade probe) was substituted by its unblocked form (gRNA or trigger DNA) at the same concentration to allow direct comparison. For the gRNA decoy and multiguide enhancement strategies, additional gRNA-T1 or gRNA-T2-310 (*SI Appendix*, Table S1) was added to the T1 reaction tube, with an equal volume removed from the water component to maintain a consistent total reaction volume and overall reagent concentrations.

Pathogen Culture. Tryptic soy broth (TSB) and agar were obtained from the Cell Media Facility at the University of Illinois Urbana–Champaign (UIUC). Methicillin-resistant *Staphylococcus aureus* (MRSA) was cultured in TSB and incubated at 37 °C for 16 h. After incubation, phosphate-buffered saline (PBS) stocks were prepared by centrifuging 1 mL of the overnight culture at 6,000× *g* for 10 min to pellet the cells. The pellet was washed twice with 1× PBS, resuspended in 1 mL PBS, aliquoted, and stored at room temperature. Stocks were used within 4 d of preparation. Colony counts were verified by plating, and appropriate dilutions were made in whole blood for experimental use.

Detection of Pathogen in Blood Sample. Venous whole blood was obtained from BIOIVT (HUMANWBK2-0101184; Human Whole Blood K^2EDTA, gender unspecified) and stored at 4 °C on a rotating mixer for up to 2 wk before experimentation. To achieve target bacterial concentrations, 10-fold serial dilutions of bacterial stocks were prepared and spiked into whole blood. Genomic DNA was extracted using the QIAamp DNA Blood Kit (QIAGEN, 51104) following the

manufacturer's protocol. Briefly, 200 μL of blood was treated with QIAGEN Protease and incubated with lysis buffer at 56 °C for 10 min. Ethanol was added to the lysate, which was then transferred to a QIAamp Mini spin column. After centrifugation, DNA bound to the column was washed sequentially with kit-provided buffers to remove impurities and subsequently eluted in 200 μL nuclease-free water by centrifugation. The sample was measured with the CRISPR-Cascade assay.

PCR. PowerTrack SYBR Green Master Mix (Thermo Fisher Scientific) was prepared following the manufacturer's protocol. qPCR reactions were conducted in a 10 μL total volume containing 1 μL of sample and 200 nM each of forward and reverse primers. A standard calibration curve was generated using MRSA genomic DNA ranging from 1 to 10^4 copies per μL in 10-fold serial dilutions. Amplification was performed on a QuantStudio3 Real-Time PCR System. Extracted DNA from whole-blood samples spiked with MRSA were classified as positive or negative based on whether their Ct values fell within the range defined by the standard calibration curve.

Use of AI. The initial draft of this manuscript was written by the authors. ChatGPT (OpenAI GPT 5, 2025 version) was used only to improve sentence clarity, grammar, and readability. All AI assisted edits were carefully reviewed and verified by the authors to ensure scientific accuracy and integrity.

Data, Materials, and Software Availability. Study data are included in the article and/or *SI Appendix*.

ACKNOWLEDGMENTS. J.L. acknowledges Material Research Lab (MRL, UIUC) for the Professor Joe Greene Postdoctoral Fellowship by Material Research Laboratory at UIUC. We acknowledge BioRender for figure creation. Figs. 1, 2 *E*, *G*, and *H*, 3*B*, 4*A*, 5*A*, and 6*A* were generated using BioRender. We thank the staff at the Holonyak Micro and Nanotechnology Laboratory at UIUC for facilitating the research and the funding from University of Illinois. The following product was obtained through BEI Resources, NIAID, NIH: NR-10320 and NR-10192. This work was partially supported by VinUni-Illinois Smart Health Center and the NIH (R01AI148385 & R01EB032725 A). E.V. and R.B. acknowledge partial support from the Jump ARCHES (Applied Research through Community Health through Engineering and Simulation) endowment through the Health Care Engineering Systems Center at UIUC and OSF.

Author affiliations: [a]Department of Bioengineering, University of Illinois at Urbana–Champaign, Urbana, IL 61801; [b]Nick Holonyak Jr. Micro and Nanotechnology Laboratory, University of Illinois at Urbana–Champaign, Urbana, IL 61801; [c]Materials Research Laboratory, University of Illinois Urbana–Champaign, Urbana, IL 61801; [d]Carl R. Woese Institute for Genomic Biology, University of Illinois at Urbana–Champaign, Urbana, IL 61801; [e]Department of Mechanical Science and Engineering, University of Illinois at Urbana–Champaign, Urbana, IL 61801; [f]Department of Electrical and Computer Engineering, University of Illinois at Urbana–Champaign, Urbana, IL 61801; [g]Department of Materials Science and Engineering, University of Illinois at Urbana–Champaign, Urbana, IL 61801; [h]Department of Biomedical and Translational Sciences, Carle Illinois College of Medicine, Urbana, IL 61801; and [i]Biohub, Chicago, IL 60642

1. J. Lim *et al.*, Microfluidic point-of-care device for detection of early strains and B.1.1.7 variant of SARS-CoV-2 virus. *Lab. Chip* **22**, 1297–1309 (2022), 10.1039/d2lc00021k.
2. J. Lim *et al.*, Point-of-care multiplex detection of respiratory viruses. *ACS Sens.* **9**, 4058–4068 (2024), 10.1021/acssensors.4c00992.
3. E. Valera *et al.*, COVID-19 point-of-care diagnostics: Present and future. *ACS Nano* **15**, 7899–7906 (2021), 10.1021/acsnano.1c02981.
4. O. O. Abudayyeh, J. S. Gootenberg, CRISPR diagnostics. *Science* **372**, 914–915 (2021), 10.1126/science.abi9335.
5. M. M. Kaminski, O. O. Abudayyeh, J. S. Gootenberg, F. Zhang, J. J. Collins, CRISPR-based diagnostics. *Nat. Biomed. Eng.* **5**, 643–656 (2021), 10.1038/s41551-021-00760-7.
6. J. S. Gootenberg *et al.*, Nucleic acid detection with CRISPR-Cas13a/C2c2. *Science* **356**, 438–442 (2017), 10.1126/science.aam9321.
7. J. P. Broughton *et al.*, CRISPR–Cas12-based detection of SARS-CoV-2. *Nat. Biotechnol.* **38**, 870–874 (2020), 10.1038/s41587-020-0513-4.
8. S. Talebian, F. Dehghani, P. S. Weiss, J. Conde, Biotechnology forum evolution of CRISPR- enabled biosensors for amplification-free nucleic acid detection. *Trends Biotechnol.* **42**, 10–13 (2023), 10.1016/j.tibtech.2023.07.004.
9. K. Shi *et al.*, A CRISPR-Cas autocatalysis-driven feedback amplification network for supersensitive DNA diagnostics. *Sci Adv.* **7**, 1–9 (2021), 10.1126/sciadv.abc7802.
10. Y. Hu *et al.*, Cell-free DNA: A promising biomarker in infectious diseases. *Trends Microbiol.* **33**, 421–433 (2025), 10.1016/j.tim.2024.06.005.
11. M. Wang *et al.*, Engineering molecular switches of CRISPR/Cas12a for biosensing applications. *Chem. Commun.* **61**, 13052–13065 (2025), 10.1039/d5cc03652f.
12. S. Zhao *et al.*, Trends in analytical chemistry engineering positive feedback in nucleic acid circuit biosensors: Design and applications. *Trends Anal. Chem.* **191**, 118367 (2025), 10.1016/j.trac.2025.118367.
13. J. Lim *et al.*, Amplification-free, OR-gated CRISPR-Cascade reaction for pathogen detection in blood samples. *Proc. Natl. Acad. Sci. U.S.A.* **120**, 2017 (2025).
14. H. Chen *et al.*, Ultrasensitive detection of clinical pathogens through a target-ampli fi cation-free CasΦ tool. *Nat Commun.* **16**, 3929 (2025), 10.1038/s41467-025-59219-x.
15. Y. Zhang, Y. Chen, Q. Zhang, Y. Liu, X. Zhang, An aM-level sensitive cascade CRISPR-Dx system (ASCas) for rapid detection of RNA without pre-amplification. *Biosens. Bioelectron.* **230**, 115248 (2023), 10.1016/j.bios.2023.115248.
16. F. Deng *et al.*, Topological barrier to Cas12a activation by circular DNA nanostructures facilitates autocatalysis and transforms DNA / RNA sensing. *Nat. Commun.* **15**, 1–16 (2024), 10.1038/s41467-024-46001-8.
17. N. Mohammad, L. Talton, Z. Hetzler, M. Gongireddy, Q. Wei, Unidirectional trans-cleaving behavior of CRISPR-Cas12a unlocks for an ultrasensitive assay using hybrid DNA reporters containing a 3′ toehold. *Nucleic Acids Res.* **51**, 9894–9904 (2023), 10.1093/nar/gkad715.
18. S. Chen *et al.*, PAM-less conditional DNA substrates leverage trans-cleavage of CRISPR-Cas12a for versatile live-cell biosensing. *Chem. Sci.* **13**, 2011–2020 (2022), 10.1039/d1sc05558e.
19. P. H. von Hippel, N. P. Johnson, A. H. Marcus, Invited review fifty years of DNA "Breathing": Reflections on old and new approaches. *Biopolymers* 99, 923–954 (2013), 10.1002/bip.22347.
20. S. K. Banik, O. Krichevsky, R. Metzler, T. Ambjo, Breathing dynamics in heteropolymer DNA. *Biophys. J.* **92**, 2674–2684 (2007), 10.1529/biophysj.106.095935.
21. J. N. Zadeh *et al.*, Software news and updates NUPACK: Analysis and design of nucleic acid systems. *J. Comput. Chem.* **32**, 170–173 (2010).
22. N. R. Markham, M. Zuker, DINAMelt web server for nucleic acid melting prediction. *Nucleic Acids Res.* **33**, 577–581 (2005), 10.1093/nar/gki591.
23. D. A. Braasch, D. R. Corey, Locked nucleic acid (LNA): Fine-tuning the recognition of DNA and RNA. *Chem. Biol.* **8**, 1–7 (2001).
24. A. Grünweller, R. K. Hartmann, Locked nucleic acid oligonucleotides the next generation of antisense agents? *BioDrugs* **21**, 235–243 (2007).
25. J. S. Chen *et al.*, CRISPR-Cas12a target binding unleashes indiscriminate single-stranded DNase activity. *Science* **360**, 436–439 (2018), 10.1126/science.aar6245.
26. D. C. Swarts, O. J. Van Der, D. C. Swarts, O. J. Van Der, M. Jinek, Structural basis for guide RNA processing and seed- Dependent DNA targeting by CRISPR-Cas12a article structural basis for guide RNA processing and seed-dependent DNA targeting by CRISPR-Cas12a.. *Mol. Cell* **66**, 221–233.e4 (2017), 10.1016/j.molcel.2017.03.016.
27. Y. Xia *et al.*, CRISPR-powered strategies for amplification-free diagnostics of infectious diseases. *Anal. Chem.* **96**, 8091–8108 (2024), 10.1021/acs.analchem.3c04363.
28. A. Ramachandran, J. G. Santiago, CRISPR enzyme kinetics for molecular diagnostics. *Anal. Chem.* **93**, 7456–7464 (2021), 10.1021/acs.analchem.1c00525.
29. E. A. Nalefski *et al.*, Kinetic analysis of Cas12a and Cas13a RNA-guided nucleases for development of improved CRISPR-based diagnostics. *iScience* **24**, 102996 (2021), 10.1016/j.isci.2021.102996.
30. P. Fozouni *et al.*, Amplification-free detection of SARS-CoV-2 with CRISPR-Cas13a and mobile phone microscopy. *Cell* **184**, 323–333.e9 (2021), 10.1016/j.cell.2020.12.001.
31. Y. Wang *et al.*, Rapid and ultrasensitive detection of Methicillin-Resistant *Staphylococcus aureus* based on CRISPR-Cas12a combined with recombinase-aided amplification. *Front. Microbiol.* **13**, 1–11 (2022), 10.3389/fmicb.2022.903298.
32. Y. Li *et al.*, Rapid one-tube RPA-CRISPR/Cas12 detection platform for methicillin-resistant Staphylococcus aureus. *Diagnostics (Basel)* **12**, 829 (2022).
33. Y. Liu *et al.*, Analytica chimica acta one-tube RPA-CRISPR Cas12a/Cas13a rapid detection of methicillin-resistant Staphylococcus aureus. *Anal. Chim. Acta.* **1278**, 341757 (2023), 10.1016/j.aca.2023.341757.
34. J. Lim *et al.*, Dried blood matrix as a new material for the detection of DNA viruses. *Adv. Healthc. Mater.* **13**, e2402506 (2024), 10.1002/adhm.202402506.
35. J. Lim *et al.*, A blood drying process for DNA amplification. *Small*. **20**, e2307959 (2023), 10.1002/smll.202307959.
36. J. Lim, K. Koprowski, M. Wester, E. Valera, R. Bashir, Review on biphasic blood drying method for rapid pathogen detection in bloodstream infections. *SLAS Technol.* **32**, 100276 (2025), 10.1016/j.slast.2025.100276.
37. A. Ganguli *et al.*, A culture-free biphasic approach for sensitive and rapid detection of pathogens in dried whole-blood matrix. *Proc. Natl. Acad. Sci. U.S.A.* **119** (2022), 10.1073/pnas.2209607119.
38. K. Sun *et al.*, An autocatalytic CRISPR-Cas amplification effect propelled by the LNA-modified split activators for DNA sensing. *Nucleic Acids Res.* **52**, 1–13 (2024), 10.1093/nar/gkae176.
39. W. He *et al.*, Split activator of CRISPR/Cas12a for direct and sensitive detection of microRNA. *Anal. Chim. Acta* **1303**, 342477 (2024), 10.1016/j.aca.2024.342477.
40. Y. Fu, J. D. Sander, D. Reyon, V. M. Cascio, J. K. Joung, Improving CRISPR-Cas nuclease specificity using truncated guide RNAs. *Nat. Biotechnol.* **32**, 279–284 (2014), 10.1038/nbt.2808.
41. C. Orosco, S. R. Rananaware, B. Huang, M. P. Hanna, M. Reza, DNA-guided CRISPR/Cas12 for RNA targeting. medRxiv [Preprint] (2024). (Accessed 25 March 2026). https://doi.org/10.1101/2024.11.21.24317744 (Accessed 25 March 2026).
42. L. Chen, M. Hu, X. Zhou, Trends in developing one-pot CRISPR diagnostics strategies. *Trends Biotechnol.* **43**, 98–110 (2024), 10.1016/j.tibtech.2024.07.007.
43. G. A. Rybnicky, R. A. Dixon, R. M. Kuhn, A. S. Karim, M. C. Jewett, Development of a freeze-dried CRISPR-Cas12 sensor for detecting *Wolbachia* in the secondary science classroom. *ACS Synth. Biol.* **11**, 835–842 (2022), 10.1021/acssynbio.1c00503.
44. Y. Tanifuji, H. Suzuki, G. Tong, Y. Hiruta, D. Citterio, Analytical Methods for application to paper-based analytical devices. *Anal. Methods* **16**, 4143–4149 (2024), 10.1039/d4ay00848k.
45. D. A. Huyke *et al.*, Enzyme kinetics and detector sensitivity determine limits of detection of amplification-free CRISPR-Cas12 and CRISPR-Cas13 diagnostics. *Anal. Chem.* **94**, 9826–9834 (2022), 10.1021/acs.analchem.2c01670.
46. A. S. Avaro, J. G. Santiago, Uncertainty quantification of Michaelis-Menten kinetic rates and its application to the analysis of CRISPR-based diagnostics. *Angew. Chem. Int. Ed. Engl.* **134**, e202209527 (2022), 10.1002/ange.202209527.

47. M. Wester, J. Lim, A. B. Van, K. Koprowski, E. Valera, Kinetic modeling of target-amplification-free CRISPR-Cas-based autocatalysis reactions. bioRxiv [Preprint] (2026). https://doi.org/10.64898/2026.03.03.709462.
48. A. Walbrun *et al.*, Single-molecule force spectroscopy of toehold-mediated strand displacement. *Nat Commun.* **15**, 7564 (2024), 10.1038/s41467-024-51813-9.
49. J. C. Cofsky *et al.*, CRISPR-Cas12a exploits R-loop asymmetry to form double-strand breaks Cas12a. *elife* **9**, e55143 (2020), https://doi.org/10.7554/eLife.55143.
50. J. Wang *et al.*, Limits in accuracy and a strategy of RNA structure prediction using experimental information. *Nucleic Acids Res.* **47**, 5563–5572 (2019), 10.1093/nar/gkz427.
51. T. Schlick, A. M. Pyle, Biophysical perspective opportunities and challenges in RNA structural modeling and design. *Biophys J.* **113**, 225–234 (2017), 10.1016/j.bpj.2016.12.037.
52. S. von Löhneysen, M. Mörl, P. F. Stadler, Limits of experimental evidence in RNA secondary structure prediction. *Front. Bioinform.* **4**, 1–6 (2024), 10.3389/fbinf.2024.1346779.